**THE EUROPEAN
PHYSICAL JOURNAL B**

Phase structure of intrinsic curvature models on dynamically triangulated disk with fixed boundary length

H. Koibuchi[a]

Department of Mechanical and Systems Engineering, Ibaraki National College of Technology, Nakane 866, Hitachinaka, Ibaraki 312-8508, Japan

Abstract. A first-order phase transition is found in two types of intrinsic curvature models defined on dynamically triangulated surfaces of disk topology. The intrinsic curvature energy is included in the Hamiltonian. The smooth phase is separated from a non-smooth phase by the transition. The crumpled phase, which is different from the non-smooth phase, also appears at sufficiently small curvature coefficient α. The phase structure of the model on the disk is identical to that of the spherical surface model, which was investigated by us and reported previously. Thus, we found that the phase structure of the fluid surface model with intrinsic curvature is independent of whether the surface is closed or open.

PACS. 64.60.-i General studies of phase transitions – 68.60.-p Physical properties of thin films, nonelectronic – 87.16.Dg Membranes, bilayers, and vesicles

1 Introduction

Triangulated surfaces are one of the basic models to investigate the physics for biological membranes and strings [1–5]. Theoretical investigations, on the basis of renormalization group strategy, have been made to reveal how the fluctuations of surfaces stiffen/soften the surface [6–10]. A considerable number of numerical studies have also been performed to understand the phase structure by using the surface simulations on fluid (or dynamical connectivity) surfaces [11–19] and on tethered (or fixed connectivity) surfaces [19–36]. The fluid model is defined on dynamically triangulated surfaces in the framework of the surface simulations, whereas the tethered model is defined on fixed connectivity surfaces. The surface simulations have relatively long history rather than that of another numerical technique Molecular Dynamics simulations for the lipid models for biological membranes [37–40]. The extrinsic curvature energy is always included in the surface Hamiltonian, because it is considered to smoother the surface. However, we must recall that the intrinsic curvature energy such as the deficit angle term can also be assumed [41–43] in the Hamiltonian because it can smoother the surface.

It has been shown recently by Monte Carlo (MC) simulations that the extrinsic curvature model of Helfrich and Polyakov-Kleinert [44–46] undergoes a discontinuous transition between the smooth phase and the crum-

pled phase on fixed connectivity spherical surfaces [28–30]. Moreover, the phase transition occurs independent of whether the Gaussian bond potential is included in the Hamiltonian or not [31]. It was also shown that the transition occurs independent of how the extrinsic curvature term is discretized [31]. It has also been reported that a tethered surface model undergoes a first-order transition, where the Hamiltonian includes an intrinsic curvature term [19–21]. The transition in this model occurs independent of whether the surface is closed or open. In fact, the transition can be observed on a sphere [19], on a disk [20], and on a torus [21].

However, it seems that many points remain to be studied in the surface models. We consider that one interesting problem is how the fluidity of lateral diffusion influences the phase transition in the model with some curvature Hamiltonian [11–19]. The phase diagram of the intrinsic curvature model was studied on dynamically triangulated spheres [19], however, it has not been studied yet on dynamically triangulated surfaces of disk topology.

If a membrane model undergoes a phase transition on dynamically triangulated surfaces, we must have reasons why such transition occurs. In fact, it is widely accepted that we can see no phase transition in the fluid membranes. The standard argument for fluid membranes is that there is no long-range order on the surface at finite bending rigidity [47].

First of all, we must not forget that the transition seems to occur on relatively small surfaces [11–14]. Even if the model in this paper undergoes a transition on small

[a] e-mail: `koibuchi@mech.ibaraki-ct.ac.jp`

surfaces, the transition may disappear on sufficiently large surfaces. Secondly, it is possible that the transition occurs without the smooth phase: the transition is not the one between the smooth phase and the crumpled phase but the one between the crumpled phase and the folded phase, which are respectively characterized by the Hausdorff dimension $2 < H < 3$ and $H \geq 3$ in the case of self-intersecting surfaces. We have some other possibilities of the origin including the argument of Helfrich that the thermal fluctuation increases the effective bending rigidity [48]. It is possible that the curvature coefficient is increased by the fluctuation of surfaces just like the case for the coefficient of the Gaussian curvature [35], which is an intrinsic curvature as well as the deficit angle term in this paper.

In this paper two types of fluid surface models are studied by MC simulations on a disk with intrinsic curvature. The Hamiltonian of the first model is a linear combination of the Gaussian bond potential and an intrinsic curvature term. The second model is a tensionless model, whose Hamiltonian is given by a linear combination of the intrinsic curvature term and a hard-wall potential, which gives only an upper bound on the bond length.

The simulations are performed under fixed total number of vertices on the boundary of disk as well as on the interior of disk. As a consequence, the mean boundary length is fixed to be $n_B \langle \ell \rangle$, where n_B is the total number of bonds on the boundary, and $\langle \ell \rangle$ is the mean bond length.

It will be shown that both models undergo a first-order transition between the smooth phase and a non-smooth phase on relatively large surfaces. Thus, we can exclude the above-mentioned first and the second possibilities of the reason for the transition in the fluid membrane model with intrinsic curvature. As a consequence, the result in this paper suggests that the fluctuation of surfaces does not always soften the surface. Thus we understand that fluidity of dynamically triangulated surfaces does not eliminate the long-range order whenever the surface model is defined with intrinsic curvature. This is in sharp contrast to the case in the model with extrinsic curvature, where the surface is softened by the surface fluctuations.

Combining the results in this paper and those in reference [19], we will confirm that the transition is independent of whether the surfaces is closed or open in fluid and intrinsic-curvature models. We consider that this result is remarkable because phase transitions are always severely influenced by boundary conditions that restrict the value of variables in statistical models.

2 Models

The starting configuration for MC simulations is a flat and regularly triangulated disk, which is obtained by dividing the hexagon. Figure 1 is a lattice of size $N = 61$, which is obtained by dividing every edge of the original hexagon into 4-pieces. By dividing the edges into L-pieces we have a lattice of $(N, N_E, N_P) = (3L^2 + 3L + 1, 9L^2 + 3L, 6L^2)$, where N, N_E, N_P are the total number of vertices, the
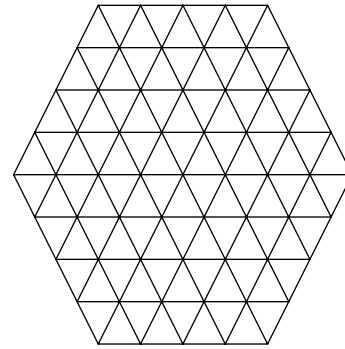
Fig. 1. A triangulated disk of size $(N, N_E, N_P) = (61, 156, 96)$, where N, N_E, N_P are the total number of vertices, the total number of edges, the total number of plaquettes (or triangles).

total number of edges, and the total number of plaquettes (or triangles).

The Gaussian bond potential S_1, the intrinsic curvature S_3, and the hard-wall potential V are given by

$$S_1 = \sum_{(ij)} (X_i - X_j)^2, \quad S_3 = \sum_i (\delta_i - \delta_0)^2,$$
$$V = \sum_{(ij)} V(|X_i - X_j|), \tag{1}$$

where $\sum_{(ij)}$ is the sum over all bonds (ij) connecting the vertices X_i and X_j, and δ_i in S_3 is the sum of angles of the triangles meeting at the vertex i. We note that $\sum_{(ij)}$ in S_1 and V include the sum over the boundary bonds. As a consequence, the length of the boundary bonds can vary in the simulations. The value of the symbol δ_0 in S_3 is given by

$$\delta_0 = \begin{cases} 2\pi & \text{(internal vertices)}; \\ \pi (\text{or } 2\pi/3) & \text{(boundary vertices)}, \end{cases} \tag{2}$$

where $2\pi/3$ is assigned to the six vertices, and π to the remaining vertices on the boundary. Because of the definition of δ_0 in (2), we can call S_3 in equation (1) as a deficit angle term.

The symbol $V(|X_i - X_j|)$ in the hard-wall potential V in equation (1) is the potential between the vertices i and j, and is defined by

$$V(|X_i - X_j|) = \begin{cases} 0 & (|X_i - X_j| < r_0), \\ \infty & (\text{otherwise}). \end{cases} \tag{3}$$

The value of r_0 in the right hand side of equation (3) is fixed to $r_0^2 = 1.08$. Then we have $\langle \sum (X_i - X_j)^2 \rangle / N \simeq 3/2$, which is satisfied when the Gaussian bond potential $S_1 = \sum (X_i - X_j)^2$ is included in the Hamiltonian, which includes no hard-wall potential such as V in equation (1).

The constraint $|X_i - X_j| < r_0$ is necessary for the bond length to have a well-defined value if the Gaussian bond potential S_1 is not included in the Hamiltonian. In fact, the size of the surface grows larger and larger in the MC simulations if it were not for the constraint $|X_i - X_j| < r_0$

in the hard-wall potential. As a consequence, the model seems to depend on a hidden length scale introduced by r_0, and then the model appears to be ill-defined. However, we checked in [18] that there is no r_0-dependence on the results. This is a consequence of the scale invariant property of the model. Therefore, we use $r_0^2 = 1.08$ in the MC simulations.

The partition function is defined by

$$Z(\alpha) = \sum_T \int \prod_{i=1}^N dX_i \exp\left[-S(X, T)\right], \qquad (4)$$

where N is the total number of vertices as described above, and $\sum_T$ denotes the summation over all possible triangulations T under a constraint which will be described in the next section. The expression $S(X, T)$ shows that S explicitly depends on the variable X and T. The coefficient α is the elastic modulus. The surfaces are allowed to self-intersect. The center of surface is fixed to remove the translational zero-mode.

Two types of models, which we call *model 1* and *model 2*, are defined by Hamiltonians

$$S(X, T) = S_1 + \alpha S_3 \qquad \text{(model 1)}, \qquad (5)$$
$$S(X, T) = V + \alpha S_3 \qquad \text{(model 2)}. \qquad (6)$$

It should be noted that the Gaussian bond potential S_1 per vertex at the internal vertices differs from the one at the boundary vertices. In fact, the co-ordination number is $q = 6$ at the internal vertices and $q = 3$ or $q = 4$ at the boundary vertices. The intrinsic curvature S_3 at the internal vertices can also be different from those at the boundary ones due to the same reason for S_1. This difference of S_1 per vertex (or S_3 per vertex) is typical to the model on the open disk, and such large difference cannot be seen in the model on closed surfaces such as a sphere or a torus. It must also be noted that the boundary is not completely free but shares both of the Gaussian bond potential (or the hard-wall potential) and the intrinsic curvature energy in the models of this paper.

We comment on a relation of S_3 in equation (1) to an intrinsic curvature energy $S_3 = -\sum_i \log(\delta_i/2\pi)$ in [19]. This S_3 in [19] is closely related with the co-ordination dependent term $S_3 = -\sum_i \log(q_i/6)$, which comes from the integration measure $\prod_i dX_i q_i^\alpha$ [49] in the partition function for the model on a sphere. $S_3 = -\sum_i \log(\delta_i/2\pi)$ has the minimum value when $\delta_i = 2\pi$ is satisfied for all i, and hence it becomes smaller on a smooth sphere than on a crumpled one. However, the flat configuration of the hexagonal lattice shown in Figure 1 does not minimize $S_3 = -\sum_i \log(\delta_i/2\pi)$, because it includes vertices such that $\delta_i \neq 2\pi$. This is the reason why we use S_3 in equation (1), which becomes zero on such flat configuration as shown in Figure 1.

3 Monte Carlo technique

The canonical Monte Carlo technique is used to update the variables X to a new X' so that $X' = X + \delta X$, where the small change δX is made at random in a small sphere in $\mathbf{R}^3$. The new position X' is accepted with the probability $\text{Min}[1, \exp(-\Delta S)]$, where $\Delta S = S(\text{new}) - S(\text{old})$. The radius δr of the small sphere is chosen at the beginning of the simulations to maintain the rate of acceptance r_X for the X-update as $0.4 \leq r_X \leq 0.6$.

The summation over T in Z of equation (4) is performed by bond flips. The bonds are labeled by sequential numbers. A bond is randomly chosen, and the flip is accepted with the probability $\text{Min}[1, \exp(-\Delta S)]$. The bond flip is applied only to internal bonds except the bonds whose both end points touch the boundary after the flip. The boundary bonds remain unflipped.

N-updates for X and N-updates for T are consecutively performed, and these make one MCS (Monte Carlo Sweep). We use a random number called Mersenne Twister [50] in the MC simulations. The above mentioned Metropolis procedure is applied only for X and T, which satisfy the constraint $|X_i - X_j| < r_0$ in equation (3) for model 2.
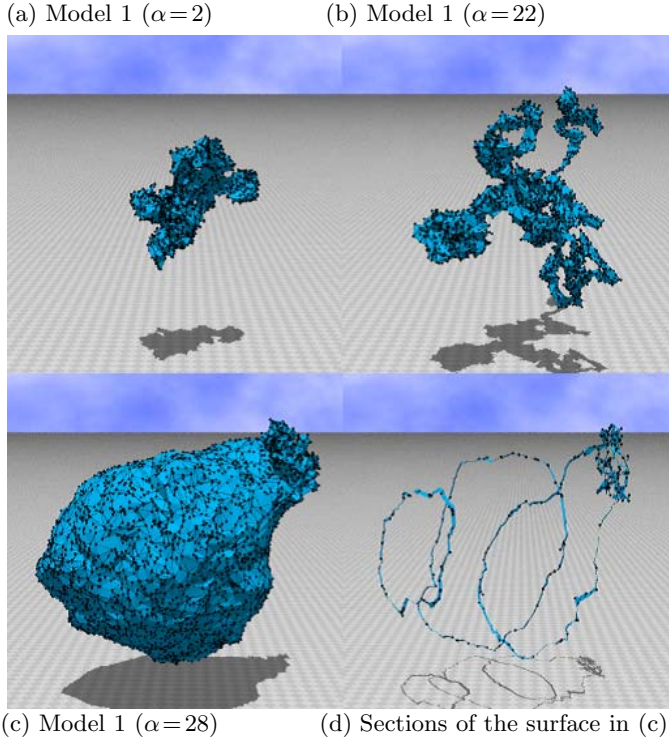
We use surfaces of size $N = 817$, $N = 1657$, $N = 3367$, and $N = 5167$, which correspond to the partitions $L = 16$, $L = 23$, $L = 33$, and $L = 41$ respectively. The size of the surfaces is relatively larger than that of spherical surfaces used in [19].

The total number of MCS after the thermalization is about $1.0 \times 10^8 \sim 3.0 \times 10^8$ in the smooth phase close to the transition point of the surfaces of size $N = 5167$, $N = 3367$, and $N = 1657$, and 1.6×10^8 for $N = 817$. Relatively smaller number of MCS ($1.0 \times 10^8 \sim 1.6 \times 10^8$) (including the thermalization MCS) is done at non-transition point. The thermalization MCS is $0.5 \times 10^7 \sim 1.0 \times 10^8$, which depends on N and α. Very large number of thermalization MCS is sometimes needed close to the transition point, because there are smooth surfaces that start to collapse into non-smooth surfaces after a long MC run. Physical quantities are calculated at every 500 MCS after the thermalization.

4 Results

Snapshots of model 1 surfaces are shown in Figures 2a–2c, which are obtained at $\alpha = 2$, $\alpha = 22$, and $\alpha = 28$, respectively. Figure 2d is a set of sections of the surface in Figure 2c. The figures are shown in the same scale, and the size is $N = 5167$. It is easy to see that the surface in Figure 2a is crumpled (or folded), and the surface in Figure 2b is a branched polymer like one. The surface in Figure 2c is obviously smooth, and it looks like a sphere with a hole. The surface in Figure 2c is separated from that in Figure 2b by a first-order transition as we will see below.

Snapshots of model 2 surfaces are shown in Figures 3a–3d, which are obtained at $\alpha = 10$, $\alpha = 32$, $\alpha = 36$, and $\alpha = 44$, respectively. The figures are shown in the same scale, and the size is $N = 5167$. It is also easy to see that the surface in Figure 3a is almost folded, and that the surface in Figure 3b is a branched polymer like one, which is rather oblong than the one in Figure 2b of model 1. The

(a) Model 1 ($\alpha=2$)   (b) Model 1 ($\alpha=22$)   (a) Model 2 ($\alpha=10$)   (b) Model 2 ($\alpha=32$)

(c) Model 1 ($\alpha=28$)   (d) Sections of the surface in (c)   (c) Model 2 ($\alpha=36$)   (d) Model 2 ($\alpha=44$)
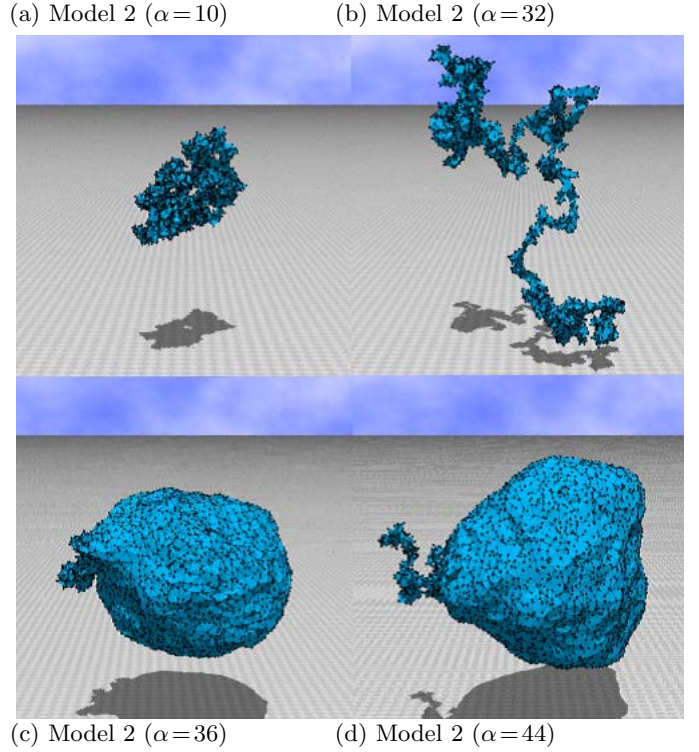

Fig. 2. Snapshots of model 1 surfaces of size $N = 5167$ at (a) $\alpha = 2$ (crumpled), (b) $\alpha = 22$ (non-smooth), and (c) $\alpha = 28$ (smooth), and (d) sections of the surface in (c). Figures are shown in the same scale.

Fig. 3. Snapshots of model 2 surfaces of size $N = 5167$ at (a) $\alpha = 10$ (crumpled), (b) $\alpha = 32$ (non-smooth), (c) $\alpha = 36$ (transient surface between non-smooth and smooth), and (d) $\alpha = 44$ (smooth). The surface in (c) is almost smooth. Figures are shown in the same scale.

snapshot in Figure 3c shows an intermediate and transient state between the non-smooth phase and the smooth phase. The reason why the surface in Figure 3c is considered to be an intermediate one is because the bending energy S_2 is relatively large, which will be shown in the next paragraph. We can see from Figure 3c that non-smooth part is almost shrunk. It is expected that the surface becomes a smooth surface after a long MC run. Because the smooth phase is separated from the non-smooth phase by first-order transition, we expect that the configuration in Figure 3c eventually belongs to the smooth phase. On the contrary, the surface in Figure 3d is almost smooth, and the non-smooth part seems to be shrunk. We note that the surface seems to be closed in the smooth phase as that in Figure 2c of model 1. The surface in Figure 3d is separated from that in Figure 3b by a first-order transition as we will see below.
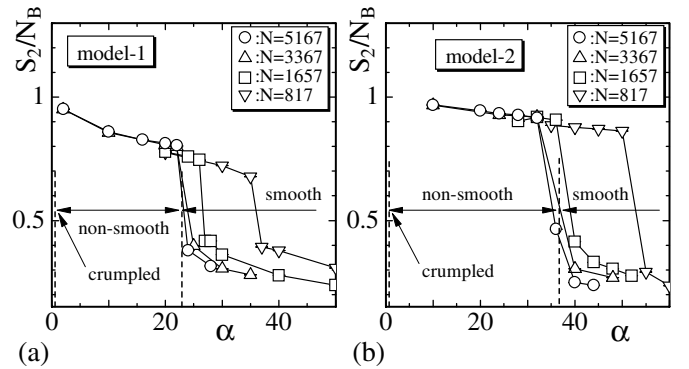
From the bending energy S_2 we can extract information about how smooth the surface is, although S_2 is not included in the Hamiltonian. The bending energy S_2 is defined by

$$S_2 = \sum_{ij} \left(1 - \mathbf{n}_i \cdot \mathbf{n}_j\right), \tag{7}$$

where $\mathbf{n}_i$ is the unit normal vector of the triangle i. The symbol ij in $\sum_{ij}$ denotes the nearest-neighbor triangles i

Fig. 4. S_2/N_B vs. α obtained in (a) model 1 and (b) model 2. N_B is the total number of internal bonds. The size of surfaces are $N = 817$, $N = 1657$, $N = 3397$, are $N = 5167$. Dashed lines denote the phase boundaries of the models on the $N = 5167$ surface.

and j, which have a common bond. The pair $\mathbf{n}_i \cdot \mathbf{n}_j$ is not defined on the boundary bonds, because we have no triangle outside the boundary.

Figures 4a and 4b are plots of the bending energy S_2/N_B against α obtained in model 1 and model 2, respectively. N_B is the total number of internal bonds. We find
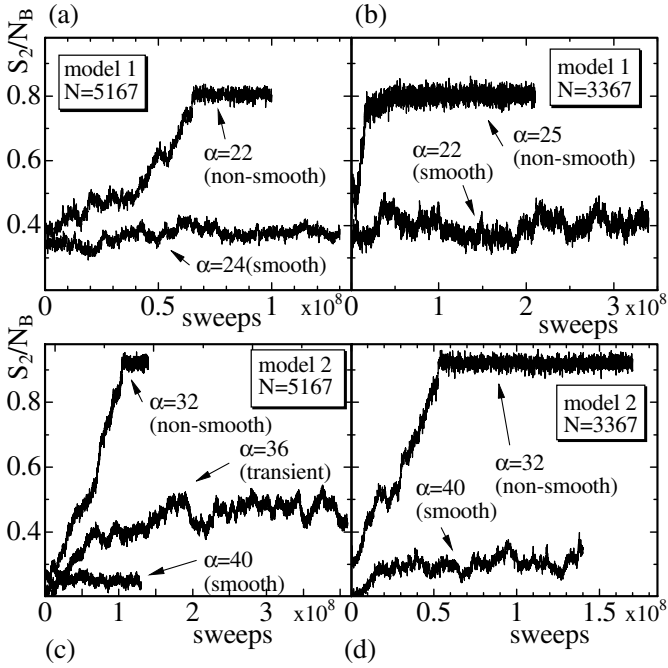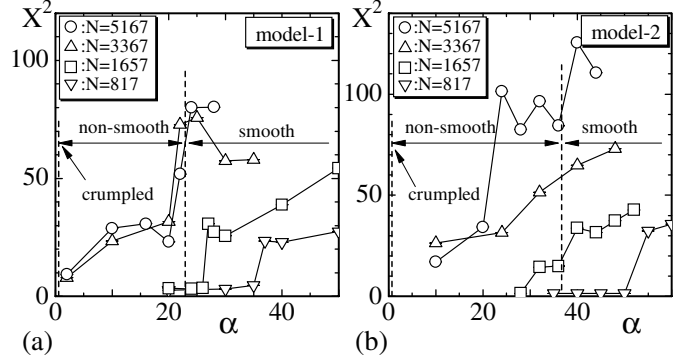
Fig. 5. Variation of S_2/N_B against MCS obtained on model 1 surface of size (a) $N = 5167$, (b) $N = 3367$, and on model 2 surface of (c) $N = 5167$, (d) $N = 3367$.

Fig. 6. X^2 vs. α obtained in (a) model 1 and (b) model 2. The size of surfaces is $N = 817$, $N = 1657$, $N = 3367$, and $N = 5167$. Dashed lines denote the phase boundaries of the models on the $N = 5167$ surface.

from Figures 4a and 4b that S_2/N_B is obviously discontinuous at finite α. Thus, we have shown that both models undergo a phase transition between the smooth phase and the non-smooth phase. As we have seen in the snapshots, both model have three different phases; the smooth, the non-smooth, and the crumpled, which is expected to emerge at sufficiently small α.

One dashed line in the figures denotes the phase boundary between the smooth phase and the non-smooth phase on the $N = 5167$ surface, and the other one denotes the phase boundary between the non-smooth phase and the crumpled phase. Since the transition point of the $N = 3367$ surface is almost identical to that of the $N = 5167$ surface, the transition seems not to be influenced by the finite-size effects in those system size. We note also that the non-smooth surfaces do not appear between the smooth phase and the crumpled phase on the $N = 817$ and $N = 1657$ surfaces. The reason of this seems due to the finite-size effect.

The order of the transitions between the smooth phase and the non-smooth one is considered as first order, because S_2/N_B is discontinuous as shown above. We recall that a phase transition is called a first-order (or discontinuous) one if some physical quantity discontinuously changes even when the quantity is not included in the Hamiltonian. On the contrary, we can see no transition between the crumpled and the non-smooth phases. In fact, S_2/N_B and some other physical quantities smoothly vary at the transition region of α, just as in the spherical surface model [19].

In order to see how is the convergence of the simulations close to the transition point, we plot the variation of S_2/N_B against MCS including the thermalization MCS in Figures 5a–5d: Figure 5a is S_2/N_B obtained at $\alpha = 22$ (non-smooth) and $\alpha = 24$ (smooth) on the $N = 5167$ surface of model 1, Figure 5b is those obtained at $\alpha = 25$ (non-smooth) and $\alpha = 22$ (smooth) obtained on the $N = 3367$ surface of model 1, Figure 5c is those obtained at $\alpha = 32$ (non-smooth), $\alpha = 36$ (transient), and $\alpha = 40$ (smooth) on the $N = 5167$ surface of model 2, and Figure 5d is those obtained at $\alpha = 32$ (non-smooth) and $\alpha = 40$ (smooth) obtained on the $N = 3367$ surface of model 2. We immediately see that the total number of MCS after the thermalization in the non-smooth phase is relatively smaller than that in the smooth phase in the $N = 5167$ surface shown in Figures 5a and 5c. The reason of this is because the value of S_2/N_B is stable in the non-smooth phase after the thermalization. On the contrary, relatively large number of MCS was performed in the smooth phase close to the transition point, because a smooth surface can collapse into a non-smooth surface after a long MC run as stated in the final paragraph of the previous section. The variation at $\alpha = 36$ (transient) in Figure 5c indicates that the surface seems belong to the smooth phase after long MC run, although the value of S_2/N_B still remains relatively larger than that of $\alpha = 40$ (smooth).

We found no variation of S_2/N_B against MCS indicating jumps from the smooth phase to the non-smooth phase and vice versa. However, the value of S_2/N_B in the non-smooth phase is quite distinct from that in the smooth phase after the thermalization. Therefore, the gaps (or discontinuities) in S_2/N_B shown in Figures 4a and 4b are considered as a sign of a discontinuous transition.

In order to see the size of surfaces, we calculate the mean square size X^2 defined by

$$X^2 = \frac{1}{N} \sum_i \left(X_i - \bar{X} \right)^2, \quad \bar{X} = \frac{1}{N} \sum_i X_i, \quad (8)$$
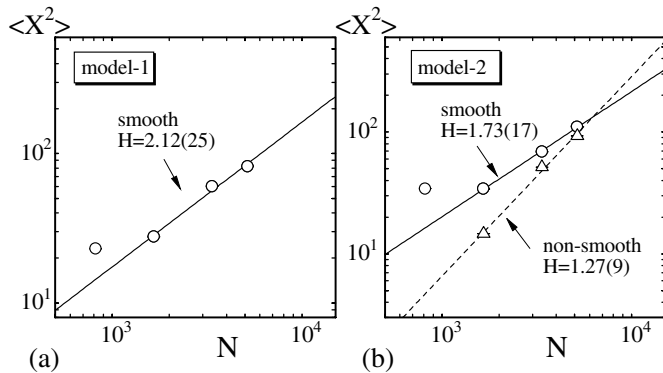
Fig. 7. (a) Log-log plots of $\langle X^2 \rangle$ vs. N ($\circ$) obtained at the smooth phase close to the transition point of model 1, (b) log-log plots of $\langle X^2 \rangle$ vs. N obtained in the smooth phase ($\circ$) and in the non-smooth phase ($\triangle$) close to the transition point of model 2. The straight lines and the dashed line are drawn by fitting the data to equation (9).

where $\bar{X}$ is the center of the surface.

We plot X^2 against α in Figures 6a and 6b obtained in model 1 and model 2, respectively. The dashed lines drawn vertically in the figures denote the phase boundaries of the $N = 5167$ surface. These lines were drawn at the same position as the corresponding dashed lines in Figures 4a and 4b. We see in Figure 6a that X^2 discontinuously changes at finite α in model 1. The transition point α, where X^2 discontinuously changes in Figure 6a, is identical to α where S_2/N_B discontinuously changes in Figure 4a. The transition point α shown in Figure 6a distinguishes the smooth phase from the non-smooth phase in model 1. This indicates that the surface in the non-smooth phase is almost crumpled.

On the contrary, these two phases can hardly be distinguished by X^2 in model 2, because X^2 in the non-smooth phase is almost comparable to X^2 in the smooth phase close to the transition point. This phenomenon is apparent on the $N \geq 1657$ surfaces and consistent with the fact that the surface of the non-smooth phase in model 2 is relatively oblong and extended as shown in Figure 3b.

Figure 7a shows log-log plots of $\langle X^2 \rangle$ against N, where $\langle X^2 \rangle$ are obtained by averaging X^2 over several points α close to the transition point with the weight of inverse error; $\alpha = 24$, $\alpha = 28$ for $N = 5167$, $\alpha = 25$, $\alpha = 30$, $\alpha = 35$ for $N = 3367$, $\alpha = 27$, $\alpha = 28$, $\alpha = 30$ for $N = 1567$, and $\alpha = 37$, $\alpha = 40$ for $N = 817$. The reason why we need such averaging of X^2 is that X^2 changes with α in the smooth phase in contrast to the case of spherical surfaces [30,31]. The straight line is obtained by fitting the largest three X^2 to

$$X^2 \sim N^{2/H}, \tag{9}$$

where H is the Hausdorff dimension. Thus we have

$$H = 2.12 \pm 0.25, \text{ (smooth)} \qquad \text{(model 1)}. \tag{10}$$
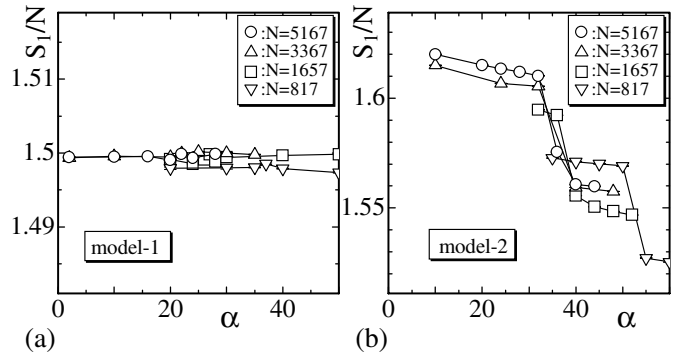
The result $H = 2.12(25)$ in equation (10) is consistent with that the surface of model 1 is almost spherical in the smooth phase, as we have seen in Figure 2c.

The Hausdorff dimension in the branched polymer phase is expected to be $H = 2$, however, we can not extract information about H in the non-smooth phase from our numerical results of model 1. One of the reason is because the non-smooth phase appears only on the surface of size $N = 3367$ and $N = 5167$, and another reason is because X^2 is not always constant against α in the non-smooth phase on those surfaces, as we can see in Figure 6a. If we could have performed very high-statistics simulations on larger surfaces, H can be obtained even in the non-smooth phase.

The solid line in Figure 7b is drawn by fitting $\langle X^2 \rangle$ in the smooth phase of model 2; they were obtained by averaging X^2 close to the transition point; $\alpha = 40$, $\alpha = 44$ for $N = 5167$, $\alpha = 40$, $\alpha = 48$ for $N = 3367$, $\alpha = 40$, $\alpha = 44$, $\alpha = 48$ for $N = 1567$, and $\alpha = 55$, $\alpha = 60$ for $N = 817$. Then, we have

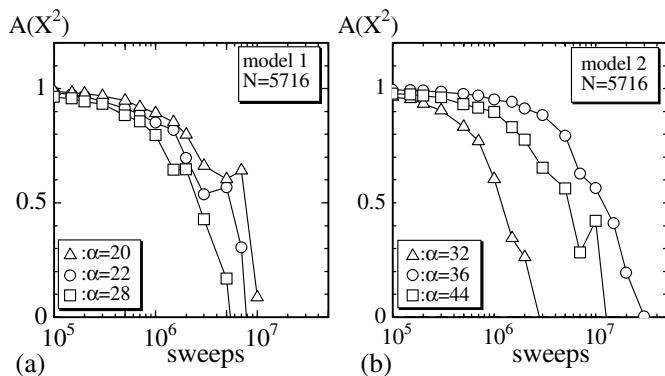$$H = 1.73 \pm 0.17, \text{ (smooth)}. \tag{11}$$

The result $H = 1.73(17)$ is considered to represent a property characteristic to the smooth phase as in the case of model 1. In fact, $H = 1.73(17)$ in (11) is close to $H = 2$, and therefore it is consistent with that the surface of model 2 is almost spherical in the smooth phase, as we have seen in Figure 3d.

The dashed line in Figure 7b is drawn by fitting $\langle X^2 \rangle$ in the non-smooth phase of model 2; they were obtained by averaging X^2 close to the transition point; $\alpha = 24$, $\alpha = 28$, $\alpha = 32$ for $N = 5167$, $\alpha = 32$ for $N = 3367$, $\alpha = 32$, $\alpha = 36$ for $N = 1567$. Then we have $H = 1.27 \pm 0.09$, which implies that the non-smooth phase seems not to be the branched polymer phase at least in model 2. The non-smooth phase seems rather close to an oblong linear surface, because $H = 1.27 \pm 0.09$ is close to $H = 1$.

Figures 8a and 8b show the Gaussian bond potential S_1/N of model 1 and model 2, respectively, although S_1 is not included in the Hamiltonian of model 2. We find from Figure 8a that the relation $S_1/N = 3/2$, which is expected

Fig. 8. (a) S_1/N vs. α for model 1, and (b) S_1/N vs. α for model 2. S_1/N has a clear jump in (b).
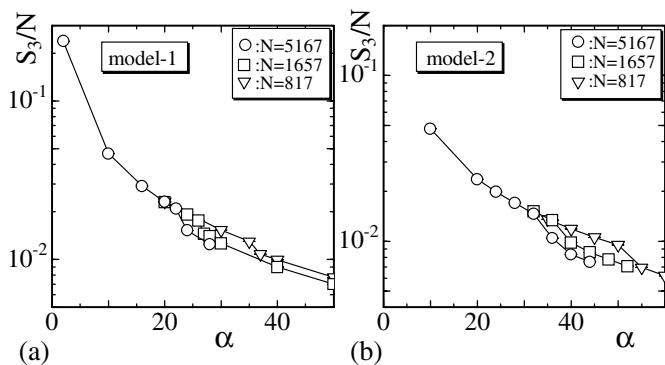
Fig. 9. (a) S_3/N vs. α for model 1, and (b) S_3/N vs. α for model 2.

Fig. 10. Auto-correlation coefficient $A(X^2)$ of (a) model 1 at $\alpha = 20$ (non-smooth), $\alpha = 22$ (non-smooth), $\alpha = 28$ (smooth phase), and (b) model 2 at $\alpha = 32$ (non-smooth), $\alpha = 36$ (transient), $\alpha = 44$ (smooth).

from the scale invariant property of the partition function of model 1, is not influenced by the first-order transition. Whereas in model 2 S_1/N discontinuously changes at the transition point, where S_2 has a gap as shown in Figure 4b. This discontinuity of S_1 also indicates that model 2 undergoes a discontinuous transition. Therefore, the discontinuous transition of model 2 is characterized by gaps of S_2 and S_1, although X^2 seems continuous at the transition point as we have seen in Figure 6b.

The intrinsic curvature energies S_3/N of model 1 and model 2 are shown in Figures 9a and 9b in a log-linear scale. The discontinuity of S_3/N is relatively unclear compared with that of S_2/N_B in Figures 4a, 4b. Nevertheless, S_3/N also changes discontinuously at the transition point in both models. Moreover, we find also that S_3/N in the crumpled phase is quite larger than those in the other phases. These indicate that that both non-smooth surface and crumpled surface are non-flat as an intrisnsic curvature surface. Thus, the non-smooth surface and the crumpled surface are non-flat both extrinsically and intrinsically.

In order to see the convergence speed of the MC simulations in both models, we plot in Figures 10a and 10b

the autocorrelation coefficient $A(X^2)$ of X^2 defined by

$$A(X^2) = \frac{\sum_i X^2(\tau_i) X^2(\tau_{i+1})}{\left[\sum_i X^2(\tau_i)\right]^2}, \qquad (12)$$

$$\tau_{i+1} = \tau_i + n \times 500, \quad n = 1, 2, ...$$

The horizontal axes in the figures represent $500 \times n$ ($n = 1, 2, ...$)-MCSs, which is a sampling-sweeps between the samples $X^2(\tau_i)$ and $X^2(\tau_{i+1})$. The coefficients $A(X^2)$ in Figures 10a and 10b are obtained on the surface of size $N = 5617$ in model 1 and model 2, respectively.

We clearly see from Figure 10a that the convergence speed in the smooth phase ($\alpha = 28$) is almost identical to that in the non-smooth phase ($\alpha = 20$), and it is also identical to that at $\alpha = 22$, which seems very close to the transition point but remains in the non-smooth phase. The reason why the convergence speed in the smooth phase is comparable to the one in the non-smooth phase is that the phase space volume ($\subseteq \mathbf{R}^3$), where the vertices X_i take their values, in the smooth phase is almost identical to that in the non-smooth phase. Figure 10b shows the coefficient $A(X^2)$ of model 2. They were obtained in the non-smooth phase ($\alpha = 32$), in the smooth phase ($\alpha = 44$), and at a transient point ($\alpha = 36$) between the two phases. We find that the convergence speed in the non-smooth phase ($\alpha = 32$) is relatively faster than that in the smooth phase in model 2.

Decorrelation MCS is about $0.3 \times 10^7 \sim 1 \times 10^7$ on the $N = 5167$ surface close to the transition point in both models, because $A(X^2) \sim 0$ at $0.3 \times 10^7 \sim 1 \times 10^7$ in Figures 10a, 10b. Therefore, the total number of MCS ($0.4 \times 10^8 \sim 1 \times 10^8$) after the thermalization, which was shown in Figures 5a–5d, is considered to be sufficient, because it is very larger than the decorrelation MCS. However, we must note that the statistics is still not so high to obtain the Hausdorff dimension in the non-smooth phase and in the smooth phase as stated before.

We should mention that phenomena of the critical slowing down in $A(X^2)$ at the transition point is very hard to see in our MC technique. The reason of this is because of very low speed of convergence. The change from the non-smooth phase to the smooth one appears to be almost irreversible. If the vertices are once trapped in a small region of $\mathbf{R}^3$ at the transition point, they hardly expand to be a smooth surface at least with the simulation technique in this paper. We obtain no series of MC data which includes configurations in the smooth phase and those in the non-smooth phase alternately even at the transition point. We consider that this irreversibility is only due to the simulation technique. These trapping phenomena were also seen in the same model on a sphere [19], which was studied by using the same simulation technique. But, the transition between the two different phases must eventually be seen after long MC simulations at α sufficiently apart from the transition point.

Finally, we comment on the coordination number of surfaces. The maximum coordination number q_{max} is $q_{max} = 22$ on the $N = 5167$ surface of model 1, and

$q_{max} = 19$ on the $N = 5167$ surface of model 2. These values of q_{max} were almost independent of α at $2 \leq \alpha \leq 28$ for model 1 and at $10 \leq \alpha \leq 44$ for model 2.

5 Summary and conclusion

The purpose of this study was to understand how the fluidity of dynamical triangulation influences the first-order crumpling transition observed in the model on the fixed connectivity disk, which is an open surface. We were also interested in that the transition is independent of whether the surface is open or closed.

Two types of fluid surface model have been investigated on a dynamically triangulated disk with intrinsic curvature; one with the Gaussian bond potential and the other with a hard-wall potential in place of the Gaussian bond potential. Both potentials are defined on all the bonds including the boundary bonds. The triangulated disk is obtained by dividing the edges of the hexagon into L-pieces, for a starting configuration of the MC simulations. The triangulated disk is characterized by $(N, N_E, N_T) = (3L^2 + 3L + 1, 9L^2 + 3L, 6L^2)$, where N_E, N_T are the total number of edges and the total number of triangles. In order to see whether the finite size effect influences the transition or not, we used surfaces of size up to $N = 5762$, which is relatively larger than those previous studies on dynamically triangulated surfaces. The boundary bonds are prohibited from flipping, and the remaining internal bonds are allowed to flip so that at least one of the two-vertices of the bond connects to an internal vertex after the flip.

We have shown that both models undergo a first-order phase transition between the smooth phase and the non-smooth phase. The transition in model 1 is characterized by a discontinuity of S_2 and that of X^2, whereas the transition in model 2 by a discontinuity of S_2 and that of S_1. Those discontinuities are considered to reflect a discontinuous transition. A phase transition is considered to be of first-order whenever some physical quantity has a gap or a jump.

The transition occurs independent of whether the Gaussian bond potential is included in the Hamiltonian or not. Surfaces appear to be spherical in the smooth phase in both models. Our results indicate that the first-order transition is not influenced by the diffusion of vertices over dynamically triangulated surfaces if the intrinsic curvature is included in the Hamiltonian as the curvature term. Moreover, the results in this paper together with that in [19] indicate that the transition is independent of whether the surface is open or closed.

It is interesting to study the model on the disk with grand canonical simulations so that the number of boundary vertices or bonds can change.

References

1. D. Nelson, *Statistical Mechanics of Membranes and Surfaces*, 2nd edn., edited by D. Nelson, T. Piran, S. Weinberg (World Scientific, 2004), p. 1
2. G. Gompper, M. Schick, *Self-assembling amphiphilic systems*, in *Phase Transitions and Critical Phenomena 16*, edited by C. Domb, J.L. Lebowitz (Academic Press, 1994), p. 1
3. M.J. Bowick, A. Travesset, Phys. Rept. **344**, 255 (2001)
4. K.J. Wiese, *Phase Transitions and Critical Phenomena 19*, edited by C. Domb, J.L. Lebowitz (Academic Press, 2000), p. 253
5. J.F. Wheater, J. Phys. A: Math. Gen. **27**, 3323 (1994)
6. F. David, E.Guitter, Europhys. Lett. **5**, 709 (1988)
7. L. Peliti, S. Leibler, Phys. Rev. Lett. **54**, 1690 (1985)
8. M.E.S. Borelli, H. Kleinert, A.M.J Schakel, Phys. Lett. A **267**, 201 (2000)
9. M.E.S. Borelli, H. Kleinert, Phys. Rev. B 63, 205414 (2001)
10. H. Kleinert, Eur. Phys. J. B **9**, 651 (1999)
11. S.M. Catterall, J.B. Kogut, R.L. Renken, Nucl. Phys. Proc. Suppl. B **99A**, 1 (1991)
12. J. Ambjorn, A. Irback, J. Jurkiewicz, B. Petersson, Nucl. Phys. B **393**, 571 (1993)
13. M. Bowick, P. Coddington, L. Han, G. Harris, E. Marinari, Nucl. Phys. Proc. Suppl. **30**, 795 (1993); M. Bowick, P. Coddington, L. Han, G. Harris, E. Marinari, Nucl. Phys. B **394**, 791 (1993)
14. K. Anagnostopoulos, M. Bowick, P. Gottington, M. Falcioni, L. Han, G. Harris, E. Marinari, Phys. Lett. B **317**, 102 (1993)
15. H. Koibuchi, Phys. Lett. A **300**, 586 (2002)
16. H. Koibuchi, N. Kusano, A. Nidaira, K. Suzuki, Phys. Lett. A **332**, 141 (2004)
17. H. Koibuchi, Eur. Phys. J. B **45**, 377 (2005)
18. H. Koibuchi, N. Kusano, A. Nidaira, K. Suzuki, M. Yamada, Phys. Lett. A **319**, 44 (2003)
19. H. Koibuchi, N. Kusano, A. Nidaira, Z. Sasaki, K. Suzuki, Eur. Phys. J. B **42**, 561 (2004)
20. M. Igawa, H. Koibuchi, M. Yamada, Phys. Lett. A **338**, 433 (2005)
21. I. Endo, H. Koibuchi, Phys. Lett. A **350**, 11 (2006)
22. M. Bowick, S. Catterall, M. Falcioni, G. Thorleifsson, K. Anagnostopoulos, J. Phys. I France **6**, 1321 (1996); M. Bowick, S. Catterall, M. Falcioni, G. Thorleifsson, K. Anagnostopoulos, Nucl. Phys. Proc. Suppl. **47**, 838 (1996); M. Bowick, S. Catterall, M. Falcioni, G. Thorleifsson, K. Anagnostopoulos, Nucl. Phys. Proc. Suppl. **53**, 746 (1997)
23. J.F. Wheater, Nucl. Phys. B **458**, 671 (1996)
24. Y. Kantor, D.R. Nelson, Phys. Rev. A **36**, 4020 (1987)
25. G. Gompper, D.M. Kroll, Phys. Rev. E **51**, 514 (1995)
26. H. Koibuchi, A. Nidaira, T. Morita, K. Suzuki, Phys. Rev. E **68**, 011804 (2003)
27. H. Koibuchi, N. Kusano, A. Nidaira, K. Suzuki, M. Yamada, Phys. Rev. E **69**, 066139 (2004)
28. J.-P. Kownacki, H.T. Diep, Phys. Rev. E **66**, 066105 (2002)
29. H. Koibuchi, Z. Sasaki, K. Shinohara, Phys. Rev. E **70**, 066144 (2004)
30. H. Koibuchi, T. Kuwahata, Phys. Rev. E **72**, 026124 (2005)

31. I. Endo, H. Koibuchi, Nucl. Phys. B **732 [FS]**, 426 (2006)
32. Y. Kantor, *Statistical Mechanics of Membranes and Surfaces*, 2nd edn., edited by D. Nelson, T. Piran, S. Weinberg (World Scientific, 2004), p. 111
33. Y. Kantor, M. Karder, D.R. Nelson, Phys. Rev. A **35**, 3056 (1987)
34. M. Bowick, A. Cacciuto, G. Thorleifsson, A. Travesset, Eur. Phys. J. E **5**, 149 (2001)
35. M.J. Bowick, *Statistical Mechanics of Membranes and Surfaces*, Second Edn., edited by D. Nelson, T. Piran, S. Weinberg (World Scientific, 2004), p. 323
36. D. Nelson, *Statistical Mechanics of Membranes and Surfaces*, Second Edn., edited by D. Nelson, T. Piran, S. Weinberg (World Scientific, 2004), p. 131
37. R. Goetz, R. Lipowsky, J. Chem. Phys. **108**, 7397 (1998)
38. H. Noguchi, M. Takatsu, J. Chem. Phys. **115**, 9547 (2001)
39. H. Noguchi, M. Takatsu, Biophys. J. **83**, 299 (2002)
40. I.R. Cooke, K. Kremer, M. Deserno, Phys. Rev. E **72**, 011506 (2005)
41. C.F. Baillie, D.A. Johnston, Phys. Rev. D **48**, (1993) 5025; Phys. Rev. D **49**, 4139 (1994)
42. C.F. Baillie, D. Espriu, D.A. Johnston, Phys. Lett. B **305**, 109 (1993)
43. C.F. Baillie, A. Irback, W. Janke, D.A. Johnston, Phys. Lett. B **325**, 45 (1994)
44. W. Helfrich, Z. Naturforsch **28c**, 693 (1973)
45. A.M. Polyakov, Nucl. Phys. B **268**, 406 (1986)
46. H. Kleinert, Phys. Lett. B **174**, 335 (1986)
47. P.G. De Gennes, C. Taupin, J. Phys. Chem. **82**, 2294 (1982)
48. H.A. Pinnow, W. Helfrich, Eur. Phys. J. E **3**, 149 (2000)
49. F. David, Nucl. Phys. B **257[FS14]**, 543 (1985)
50. M. Matsumoto, T. Nishimura, ACM Trans. on Modeling and Computer Simulation, Vol. 8, No. 1, January, pp. 3–30 (1998)